RESEARCH ARTICLE

A Kinetically Stabilized Nitrogen-Doped Triangulene Cation: Stable and NIR Fluorescent Diradical Cation with Triplet Ground State

Shinobu Arikawa,[a] Akihiro Shimizu,*[a,b] Daisuke Shiomi,[c] Kazunobu Sato,*[c] Takeji Takui,[c] Hikaru Sotome,*[d] Hiroshi Miyasaka,[d] Masahito Murai,[e] Shigehiro Yamaguchi,[e,f] and Ryo Shintani*[a,b]

[a] S. Arikawa, Dr. A. Shimizu, Prof. Dr. R. Shintani
Division of Chemistry, Department of Materials Engineering Science, Graduate School of Engineering Science, Osaka University, Toyonaka, Osaka 560-8531 (Japan)
E-mail: shimizu.akihiro.es@osaka-u.ac.jp
shintani.ryo.es@osaka-u.ac.jp
[b] Dr. A. Shimizu, Prof. Dr. R. Shintani
Innovative Catalysis Science Division, Institute for Open and Transdisciplinary Research Initiatives (ICS-OTRI), Osaka University, Suita, Osaka 565-0871 (Japan)
[c] Dr. D. Shiomi, Prof. Dr. K. Sato, Prof. Dr. T. Takui
Department of Chemistry, Graduate School of Science, Osaka Metropolitan University, Sumiyoshi-ku, Osaka 558-8585 (Japan)
E-mail: sato@omu.ac.jp
[d] Dr. H. Sotome, Prof. Dr. H. Miyasaka
Division of Frontier Materials Science and Center for Advanced Interdisciplinary Research, Graduate School of Engineering Science, Osaka University, Toyonaka, Osaka 560-8531 (Japan)
E-mail: sotome@laser.chem.es.osaka-u.ac.jp
[e] Dr. M. Murai, Prof. Dr. S. Yamaguchi
Department of Chemistry, Graduate School of Science, and Integrated Research Consortium on Chemical Sciences (IRCCS), Nagoya University, Furo, Chikusa, Nagoya 464-8602 (Japan)
[f] Prof. Dr. S. Yamaguchi
Institute of Transformative Bio-Molecules (WPI-ITbM), Nagoya University, Furo, Chikusa, Nagoya 464-8601 (Japan)

Abstract: A kinetically-stabilized nitrogen-doped triangulene cation derivative has been synthesized and isolated as the stable diradical with a triplet ground state that exhibits near-infrared emission. As was the case for a triangulene derivative we previously synthesized, the triplet ground state with a large singlet-triplet energy gap was experimentally confirmed by magnetic measurements. In contrast to the triangulene derivative, the nitrogen-doped triangulene cation derivative is highly stable even in solution under air and exhibits near-infrared absorption and emission because the alternancy symmetry of triangulene is broken by the nitrogen cation. Breaking the alternancy symmetry of triplet alternant hydrocarbon diradicals by a nitrogen cation would therefore be an effective strategy to create stable diradicals possessing magnetic properties similar to the parent hydrocarbons but with different electrochemical and photophysical properties.

Introduction

Luminescent organic molecules have been widely explored due to their utilities in organic light-emitting diodes (OLEDs) and sensing devices.[1,2] In addition to typical closed-shell molecules, emissive monoradicals have also been actively investigated in recent years,[3–5] most of which are triphenylmethyl radical derivatives (Figure 1a)[6–17] by breaking the alternancy symmetry of the parent triphenylmethyl radical.[18] On the other hand, studies on emissive diradicals with a triplet ground state are very limited presumably because of the difficulty in the design and synthesis of stable triplet-ground-state diradicals with a rigid structure to suppress non-radiative transitions.[19–26] In fact, only two such examples have been reported to date as far as we are aware. One is an *in-situ* generated trimethylenemethane (TMM) diradical intermediate by Ikeda et al.,[27] and the other is a stable borocyclic diradical by Wang et al. (Figure 1b),[28] which showed weak anti-Kasha fluorescence in the visible light region (λ_{max} = 420 nm with two bands at 433 and 495 nm) with a quantum yield of 0.30%.[29]

Recently, our group has been focusing on the design and synthesis of polycyclic hydrocarbons with a triplet ground state,[30,31] and succeeded in the isolation of kinetically stabilized triangulene derivative **1b** in a crystalline form, experimentally confirming its triplet ground state with a large singlet-triplet energy gap (ΔE_{ST}) of >300 K (Figure 1c).[32,33] **1b** showed only moderate stability against air and very weak absorption corresponding to the symmetry-forbidden $T_0 \rightarrow T_1$ transition and hence would not be suitable as an emissive diradical despite its rigid core structure (Figure S1). We imagined that replacement of an appropriate carbon atom of triangulene (**1a**)[30,32,34–37] with a heteroatom would increase the stability and break its alternancy symmetry to make the $T_0 \rightarrow T_1$ transition allowed while keeping its triplet ground state with a large ΔE_{ST}, thereby providing a new platform for a stable emissive diradical with a triplet ground state involving a $T_1 \rightarrow T_0$ process.

On the basis of these backgrounds, herein we describe the synthesis, isolation, and characterization of a nitrogen-doped triangulene cation derivative $\mathbf{2b}^+$ as the first stable diradical with a triplet ground state that exhibits near-infrared emission.

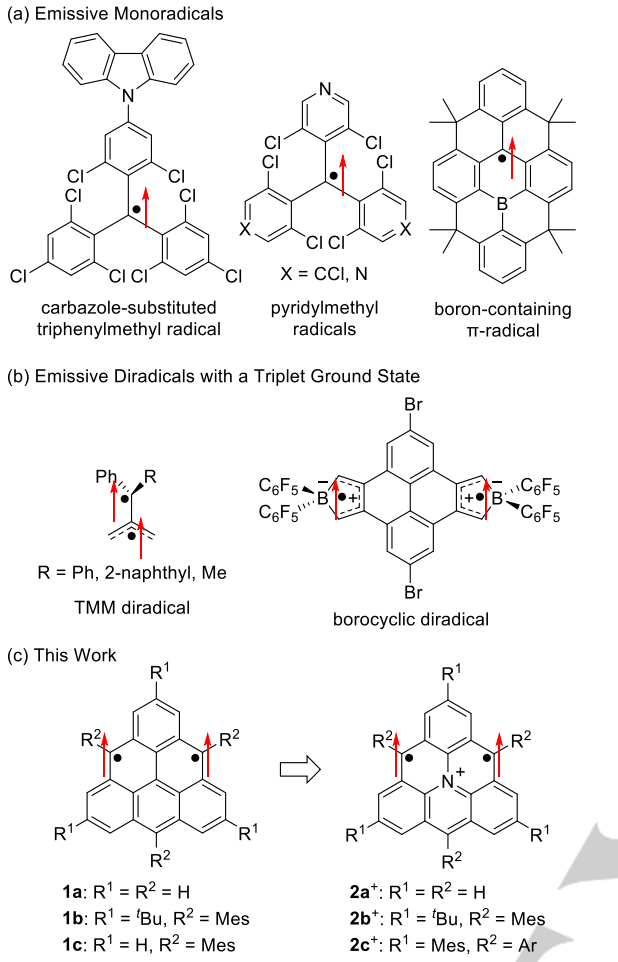

Figure 1. (a) Representative examples of emissive monoradicals. (b) Emissive diradicals with a triplet ground state. (c) Structures of **1** and **2**$^+$. Mes = 2,4,6-$Me_3C_6H_2$. Ar = 2,4,6-$Cl_3C_6H_2$.

Results and Discussion

Molecular Design

To maintain the characteristic magnetic properties of **1a**, we decided to replace the central carbon atom of **1a**, which has no coefficient in two degenerate highest occupied molecular orbitals (HOMOs, α-HOMO-A and α-HOMO-B, Figures 2a and 2b). To increase the stability toward oxygen, we chose a nitrogen cation as replacement and designed a nitrogen-doped triangulene cation **2a**$^+$, which is isoelectronic to **1a** (Figure 1c).[38] During our study, Wang et al. reported the generation of **2a**$^+$ on Au surface under ultra-high vacuum at 4 K and showed that **2a**$^+$ has a triplet ground state.[39] In addition, Wu et al. reported on the solution-phase synthesis of its derivative **2c**$^+$, but the observed electron spin resonance (ESR) spectra are more consistent with the corresponding monohydrogenated radical cation (**2c-H**$^+$) rather than **2c**$^+$ (see the Supporting Information for details).[40] Therefore, further studies toward the isolation of **2a**$^+$ or its derivatives would be necessary to understand their optical, electrochemical, and detailed magnetic properties.

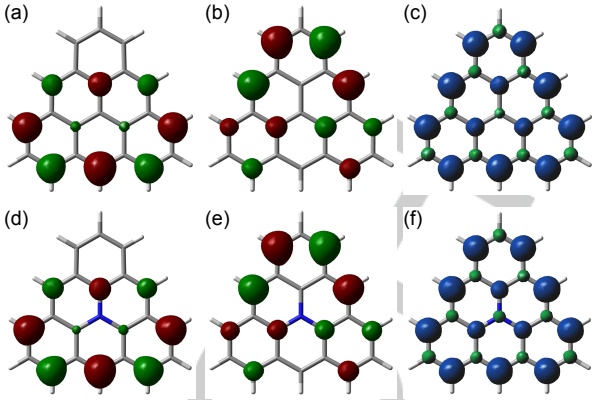

Figure 2. α-HOMO-A and α-HOMO-B of **1a** (a, b) and **2a**$^+$ (d, e) calculated at the UB3LYP/6-311G(d,p) level of theory. Spin densities of **1a** (c) and **2a**$^+$ (f) calculated at the UBLYP/6-311G(d,p)//UB3LYP/6-311G(d,p) level of theory.

Density functional theory (DFT) calculations at the B3LYP/6-311G(d,p) level of theory show that **2a**$^+$ has degenerate α-HOMOs (Figures 2d and 2e) and spin densities similar to those of **1a** (Figures 2c and 2f). As is the case for **1a** (+55.9 kJ mol^{-1}), triplet-ground-state **2a**$^+$ is expected to have a large ΔE_{ST} of +53.5 kJ mol^{-1} compared to the open-shell singlet state (which is lower in energy than the closed-shell singlet state by 63.6 kJ mol^{-1}). Introduction of the nitrogen cation in place of the central carbon atom of **1a** does not significantly affect the HOMOs of α spins (α-HOMOs) and the lowest-unoccupied molecular orbitals of β-spin (β-LUMOs), but affects the α-LUMO and β-HOMO because these orbitals have a coefficient on the central carbon atom (Figure S2, vide infra). As a result, the nitrogen cation at this position breaks the alternancy symmetry of **1a**. To kinetically stabilize the carbon atoms with large spin densities for the synthesis and isolation, we designed **2b**$^+$ having bulky *tert*-butyl and mesityl groups at the same positions as **1b** (Figure 1c).

Synthesis and Structural Characterization

The synthesis of **2b**$^+$·TfO$^-$ was achieved in three steps from tris(2-bromo-4-(*tert*-butyl)phenyl)amine (**3**)[41] (Scheme 1). Lithiation of tribromide **3** with *n*-butyllithium followed by the reaction with mesitaldehyde gave triol **4**. Intramolecular three-fold Friedel–Crafts reaction of **4** using trifluoroacetic acid gave **5** as a single isomer in 46% yield over two steps from **3**. Finally, **2b**$^+$·TfO$^-$ was synthesized by the dehydrogenation and oxidation of **5** with chloranil followed by the counter anion exchange using trifluoromethanesulfonic acid. **2b**$^+$·TfO$^-$ was purified by gel permeation chromatography followed by recrystallization from CH_2Cl_2–hexane solution in a degassed sealed tube and obtained as brown crystals in 61% yield. **2b**$^+$·TfO$^-$ was stable in a glove box under argon in the solid state and relatively stable in solution under air (vide infra).

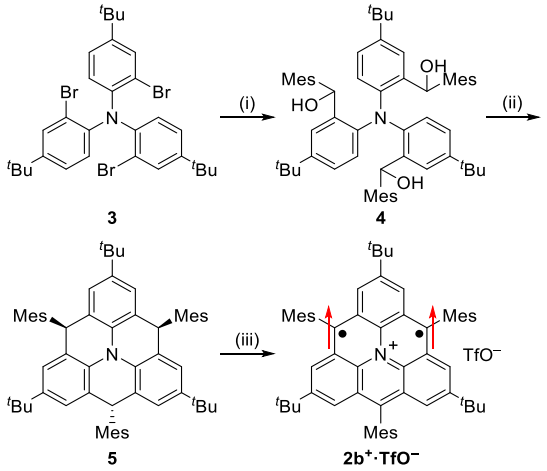

Scheme 1. Synthetic Route to **2b**$^+$·TfO$^-$. Reaction Conditions: (i) 1) ^{n}BuLi, THF, –78 °C, 1 h; 2) MesCHO, –78 °C, then RT, 1 h. (ii) CF_3CO_2H, CH_2Cl_2, –78 °C, 20 min, then RT, 30 min, 46% (two steps). (iii) 1) chloranil, CH_2Cl_2, RT, 3 h; 2) 1.0 M aq. TfOH, 61%.

Single crystals of **2b**$^+$·TfO$^-$ suitable for X-ray crystal structural analysis were obtained by recrystallization from THF–hexane (Figures 3a and S5). The dihedral angles between the mesityl groups and the main core structure are 76.0–89.5°, indicating the small electronic perturbation of mesityl groups to the core structure. No π-π interaction between **2b**$^+$ was observed because of the existence of bulky substituents and counter anion TfO$^-$, located above the main core structure of **2b**$^+$ (Figure S5), indicating the absence of significant intermolecular magnetic interaction. The main core structure of **2b**$^+$ has almost D_{3h} symmetry with the bond lengths similar to those obtained by DFT calculations at the UB3LYP/6-311G(d,p) level of theory (Figure 3a). The lengths of C–C bonds of the main core structure (*a*–*d*) of **2b**$^+$ are similar to those of **1b** within 0.012 Å.[30] The C–N bond (*e*) of **2b**$^+$ has a small double bond character on the basis of its length (1.393 Å), which is between those of triphenylamine (1.418 Å)[42] and the acridinium moiety of a 10-phenylacridinium derivative (1.372 Å),[43] and the Wiberg bond index (WBI)[44] of 1.111 obtained by the natural bonding orbital (NBO) analysis (Figure 3b).[45] The nucleus independent chemical shift (NICS)[46–48] values (NICS(1)$_{zz}$) of rings **A** and **B** of **2b**$^+$ are –11.3 and –1.9 ppm, respectively (Figure 3b). In addition, the anisotropy of the induced current density (ACID)[49,50] plot of **2b**$^+$ shows that the diatropic ring current exists in ring **A** (Figure S6). These results indicate that ring **A** is aromatic, while ring **B** is nonaromatic, which is in sharp contrast to **1b** having the same degree of aromaticity for rings **A** and **B**.[30] The electrostatic potential (ESP) surface shows that the positive charge of **2b**$^+$ located not only near the nitrogen atom but also on *γ*-carbons (Figures 3c and S7).

Based on these results, **2b**$^+$ would be described by the resonance structures **I'**, **I''**, and **I'''** with three Clar's aromatic sextets, an amine moiety, and two unpaired electrons and a positive charge localized on *γ*-carbons, and **II'**, **II''**, and **II'''** with one Clar's aromatic sextet, a pyridinium moiety, and two unpaired electrons delocalized over the periphery of **2b**$^+$ (Figure 3d). The contribution of **I'**, **I''**, and **I'''** would be due to the delocalization of positive charge and weak aromaticity of pyridinium compared to benzene.

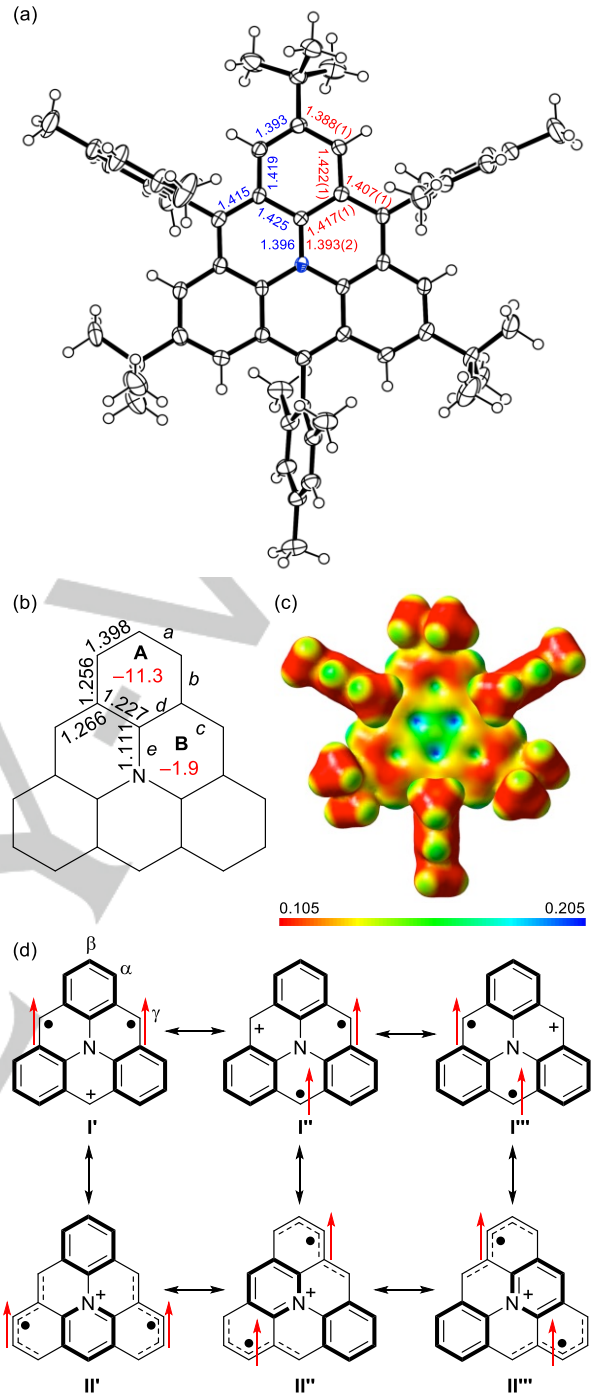

Figure 3. (a) ORTEP drawing of **2b**$^+$·TfO$^-$ at 113 K and observed (red) and calculated (blue) bond lengths (Å, mean value). Displacement ellipsoids are drawn at the 50% probability level. TfO$^-$ is omitted for clarity. (b) Wiberg bond indices (black, mean value) and NICS(1)$_{zz}$ values (ppm, red, mean value) of **2b**$^+$. (c) Electrostatic potential surface of **2b**$^+$. (d) Resonance structures of **2a**$^+$.

ESR and Magnetic Measurements

To examine the magnetic property of **2b**$^+$, we measured the continuous-wave (cw) ESR spectrum of **2b**$^+$·TfO$^-$ in benzene at room temperature, which showed a signal with a *g*-value of 2.0024 split by six equivalent protons and a nitrogen atom (Figure 4a). The hyperfine coupling constants of a_H and a_N obtained by

simulation are 10.08 and 3.61 MHz, respectively. The spin density of α-carbons of **2b**$^+$ estimated using McConnell's equation[51] (proportional constant = –66.9 MHz)[52] is 0.300 for two electrons (Figure 4b), which is in good agreement with the spin density (ρCα = 0.281, mean value) calculated at the UBLYP/6-311G(d,p)//UB3LYP/6-311G(d,p) level of theory (Figure 4b). Because the observed and calculated spin densities of the α-carbons of **2b**$^+$ are similar to those of **1b** (obs: 0.293,[30] calc: 0.283), nitrogen-doped **2b**$^+$ retains the characteristic magnetic properties of pristine **1b** (Figure S2).

In addition, similarly to **1b**, the cw ESR spectrum of **2b**$^+$·TfO$^-$ in frozen 2-methyltetrahydrofuran (2-MeTHF) showed no fine structure (Figure S8a) and the forbidden transition of ΔMs = ±2 at the half-field (Figure S8b). The triplet state of **2b**$^+$·TfO$^-$ was therefore confirmed by pulse ESR-based two-dimensional electron spin transient nutation (2D-ESTN).[53,54] The field-swept 2D-ESTN spectra of **2b**$^+$·TfO$^-$ in frozen 2-MeTHF at 10 K gave peaks at 14.5 MHz (Figure 4c), which are assigned to the triplet species judging from the ratio to a nutation frequency of the coal (10.6 MHz) used as an external standard (Figure S9). This result strongly suggests the successful observation of the triplet state of **2b**$^+$·TfO$^-$.

The zero-field splitting (ZFS) parameters determined from the ESR spectrum of **2b**$^+$·TfO$^-$ dispersed in the precursor of **1b** (Figure S10a) are $|D|$ = 0.0012 cm^{-1} and $|E|$ = 0.0003 cm^{-1} (g = 2.0026). The weak forbidden transition of ΔMs = ±2 is consistent with the small $|D|$ value (Figure S10b). Although the reason for the small $|D|$ values of **1b** and **2b**$^+$·TfO$^-$ with strong ferromagnetic interaction is still not clear, Juríček et al. also reported the small $|D|$ value for 4,8,12-trimesityltriangulene (**1c**) and could not observe its forbidden transition of ΔMs = ±2.[32] In addition, triazananographene triradical with a quartet ground state reported by Rajca et al.[55] also has a small $|D|$ value. Current DFT calculations also do not reproduce the experimental ZFS parameters of **1b** and **2b**$^+$. It is known that current theoretical approaches to ZFS tensors of highly π-delocalized high-spin systems give overestimates.[56] The experimental results may be indicative of the importance of considering electron correlation in the theoretical calculations of the ZFS tensors.

To determine the ground spin state of **2b**$^+$·TfO$^-$, the magnetic susceptibility (χ_p) was measured using a superconducting quantum interference device (SQUID) (Figure 4d). The $\chi_p T$–T plots of a microcrystalline sample of **2b**$^+$·TfO$^-$ showed the constant value of 0.97 emu K mol^{-1} at 50–300 K. Because it is very close to the value (1.00 emu K mol^{-1}) for diradicals in a triplet ground state and larger than the maximum value (0.75 emu K mol^{-1}) for diradicals with a singlet ground state, the triplet ground state of **2b**$^+$·TfO$^-$ was experimentally confirmed. Deviations of $\chi_p T$ from the value expected for S = 1 were observed below 50 K, which would be ascribed to the absorbed oxygen[57] on the surface of the sample of **2b**$^+$·TfO$^-$ in the degassed sealed tube (Figure S11). As was the case for **1b**, these results show that **2b**$^+$·TfO$^-$ has a triplet ground state with a large exchange interaction of unpaired electrons (J/k_B >> 300 K), which is consistent with the calculated ΔE_{ST} value of +51.6 kJ mol^{-1} for **2b**$^+$, and the population of thermally-excited singlet state of **2b**$^+$ at 300 K is negligible.

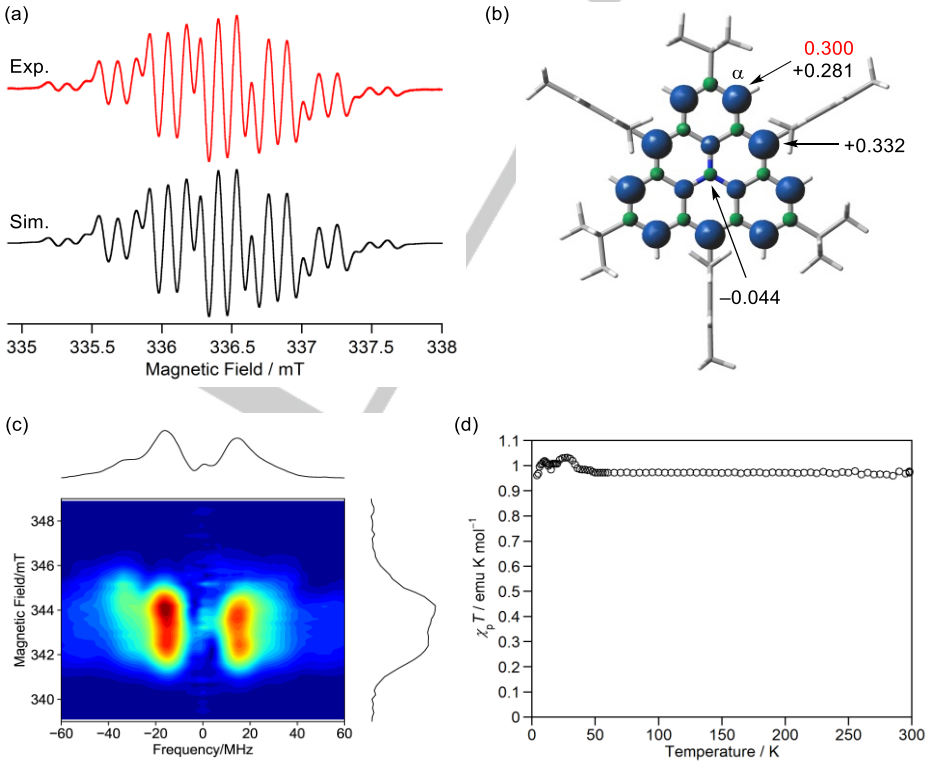

Figure 4. (a) cw ESR spectra of **2b**$^+$·TfO$^-$ in benzene at room temperature (black: experiment, red: simulation using $|a_H|$ = 10.08 MHz (6H) and $|a_N|$ = 3.61 MHz (1N)). (b) Obtained (red) and calculated (black, mean value) spin densities, and the total spin densities of **2b**$^+$ (blue and green surfaces represent α and β spin densities, respectively) calculated at the UBLYP/6-311G(d,p)//UB3LYP/6-311G(d,p) level of theory with an isovalue of 0.004. (c) X-band pulse ESR-based two-dimensional electron spin transient nutation spectra of **2b**$^+$·TfO$^-$ with a microwave irradiation strength of 6 dB in frozen 2-MeTHF solution at 10 K. (d) $\chi_p T$–T curves of **2b**$^+$·TfO$^-$.

Electrochemical and Photophysical Properties

Having established the similar magnetic properties of **2b**$^+$ compared with **1b**, we investigated its electrochemical and photophysical properties to understand the characteristic features originating from the doped nitrogen cation. In the cyclic voltammogram and differential pulse voltammogram of **2b**$^+$·TfO$^-$ in CH_2Cl_2 (Figure 5a), reversible redox waves corresponding to one-electron oxidation to **2b**$^{2+}$ (E^1_{ox} = +0.40 V vs. Fc/Fc$^+$) and one-electron reductions to **2b** (E^1_{red} = −0.96 V) and **2b**$^-$ (E^2_{red} = −1.66 V) were observed. The first oxidation and reduction potentials of **2b**$^+$ are higher than those of **1b** (E^1_{ox} = −0.24 V and E^1_{red} = −1.71 V), which indicates that the nitrogen cation lowers the energy of the α-HOMOs of **2b**$^+$, making **2b**$^+$·TfO$^-$ more stable than **1b**. Meanwhile, the energies of the on-site Coulomb repulsion of **2b**$^+$·TfO$^-$ (1.44 eV) and **1b** (1.47 eV) estimated by the difference between the oxidation and reduction potentials are very close, suggesting that **2b**$^+$ and **1b** have the same degree of delocalization of unpaired electrons.

In the UV-Vis-NIR absorption spectrum, **2b**$^+$·TfO$^-$ showed an absorption band at 815 nm in CH_2Cl_2 (Figure 5b) assigned to the symmetry-allowed $T_0 \rightarrow T_1$ transition originating from degenerate α-HOMOs → α-LUMO (770 nm, f = 0.0556) (Table S5), which is longer and stronger than the forbidden transitions between the frontier molecular orbitals of **1b** (450–650 nm). The absorption wavelength slightly shifted to shorter wavelength in C_6H_5Cl (788 nm) and CH_3CN (790 nm) (Figure 5c). Although the reason is not clear, this might be due to solvation of **2b**$^+$. It is important to note that, when the solution of **2b**$^+$·TfO$^-$ in CH_2Cl_2 was exposed to air

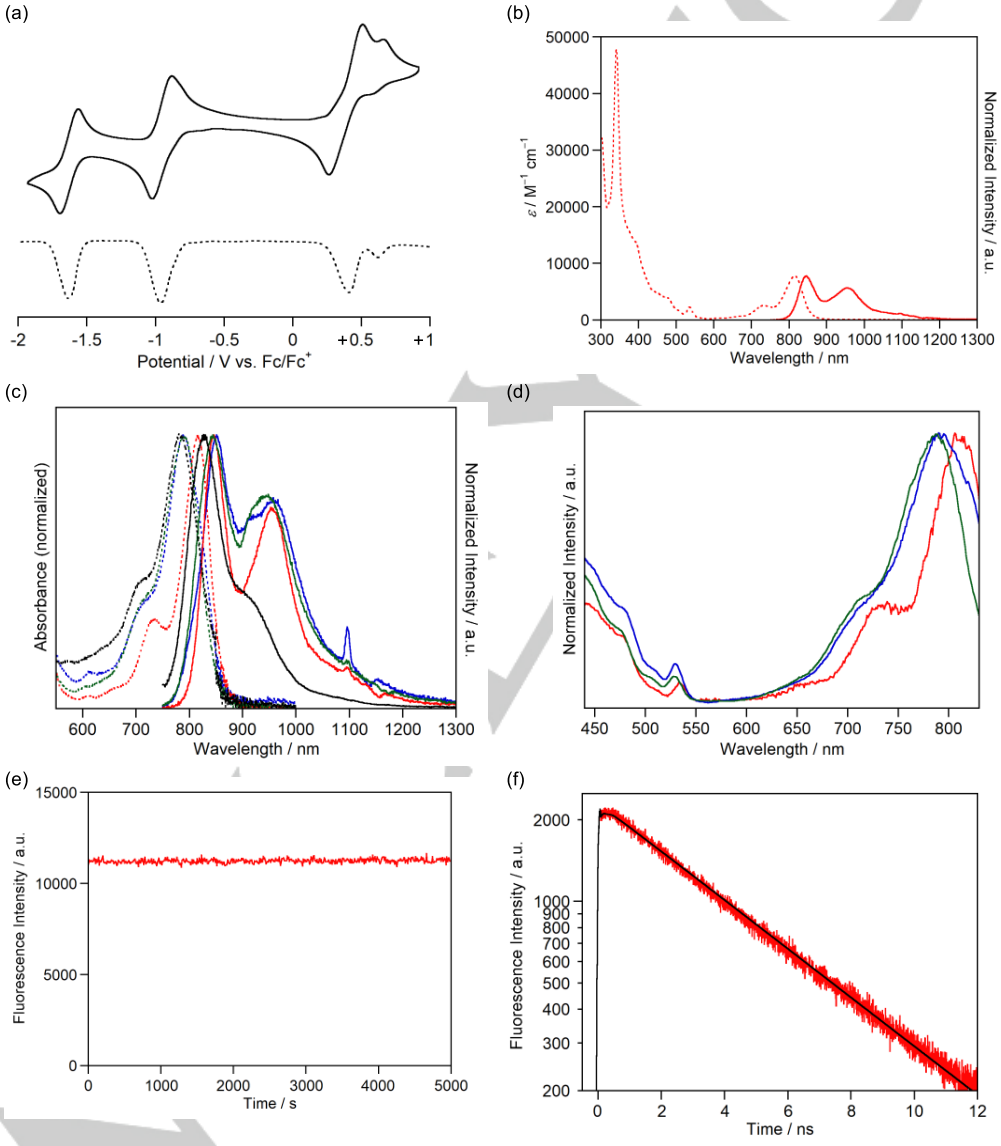

Figure 5. (a) Cyclic voltammogram (solid line) and differential pulse voltammogram (dashed line) of **2b**$^+$·TfO$^-$ in CH_2Cl_2. (b) UV-Vis-NIR absorption (dashed line) and fluorescence (solid line, excited at 730 nm) spectra of **2b**$^+$·TfO$^-$ in CH_2Cl_2. (c) UV-Vis-NIR absorption (dashed line) and fluorescence (solid line) spectra of **2b**$^+$·TfO$^-$ in CH_2Cl_2 (red), C_6H_5Cl (blue), CH_3CN (green), and PMMA (black). (d) Fluorescence excitation spectra of **2b**$^+$·TfO$^-$ in CH_2Cl_2 (red), C_6H_5Cl (blue), and CH_3CN (green) recorded at 850 nm. (e) Fluorescence intensity of **2b**$^+$·TfO$^-$ in CH_2Cl_2 solution plotted as a function of photoirradiation time. Femtosecond laser pulses at 800 nm were irradiated to the sample solution and the fluorescence was monitored at 820 nm. The irradiation power was set to 1.59 mW. The sample solution was treated by nitrogen bubbling for 15 min. (f) Fluorescence decay curve of **2b**$^+$·TfO$^-$ in CH_2Cl_2 solution monitored at 820 nm. The fluorescence lifetime was evaluated as 4.81 ns.

at room temperature, no significant change of the absorption spectra was observed for 10 h, confirming the high stability of **2b**$^+$·TfO$^-$ (Figure S13). Furthermore, **2b**$^+$·TfO$^-$ exhibited a near-infrared (NIR) fluorescence at 846 nm in CH_2Cl_2 with a small Stokes shift of 450 cm^{-1}, indicating the rigid core structure of **2b**$^+$ (Figures 5b and S14). The similar dipole moments of T_0 and T_1 states of **2a**$^+$ (T_0: 0.00 D and T_1: 0.02 D, UB3LYP/6-311G(d,p) level of theory) are consistent with the small Stokes shift. The agreement between the absorption and fluorescence excitation spectra confirmed that the detected fluorescence surely originates from **2b**$^+$·TfO$^-$ (Figure 5d). This represents the first example of an emissive triplet-ground-state diradical in the NIR region. It should be noted that **2b**$^+$·TfO$^-$ showed no decomposition under the photoirradiation condition for 5000 s (Figure 5e), indicating its ultrahigh stability under inert atmosphere. In addition, the fluorescence wavelengths and quantum yields of **2b**$^+$·TfO$^-$ were not significantly affected by polarity of the solvents (CH_2Cl_2 (846 nm, 1.3%), C_6H_5Cl (851 nm, 1.2%), and CH_3CN (844 nm, 1.2%)), which is in sharp contrast to the reported donor-acceptor NIR fluorescent molecules (Figure 5c).[58] Moreover, **2b**$^+$·TfO$^-$ (1 wt%) dispersed in poly(methyl methacrylate) (PMMA) film showed an absorption band at 781 nm and a fluorescence band at 827 nm with a quantum yield of 1.8% (Figure 5c), indicating that **2b**$^+$·TfO$^-$ would be used in emission devices. The transient absorption spectra of **2b**$^+$·TfO$^-$ in CH_2Cl_2 showed positive and negative (> 720 nm) bands up to the nanosecond time region (Figure S15). The negative band is a superposition of ground state bleaching and stimulated emission of the T_1 state, which is consistent with the absorption and fluorescence spectral shapes in Figure 5c. The lifetime of the T_1 state was quantitatively determined as 4.8 ns from the fluorescence decay curve (Figure 5f). The radiative and non-radiative rates for the $T_1 \rightarrow T_0$ transition were determined as k_r = 2.7 x 10^6 s^{-1} and k_{nr} = 2.1 x 10^8 s^{-1}. Although k_r tends to become smaller for the same oscillator strength in the NIR region, the reasonably large k_r value of **2b**$^+$·TfO$^-$ could lead to fluorescence emission in this region. The value of k_{nr} is as small as that of typical fluorescent dyes, which probably originates from the rigid core structure of **2b**$^+$.

To obtain detailed information about the allowed transition of **2b**$^+$·TfO$^-$ at NIR region, we conducted the DFT calculations of **1a** and **2a**$^+$. The energy differences between the α-HOMO and α-LUMO (3.73 eV) and the β-HOMO and β-LUMO (3.71 eV) of **1a** are similar with each other because **1a** is an alternant hydrocarbon,[59,60] and its $T_0 \rightarrow T_1$ transition is symmetry-forbidden (Figure 6a and Table S2). Because the α-LUMO and β-HOMO of **1a** have a coefficient on the central carbon atom, the energy levels of the corresponding orbitals of **2a**$^+$ (α-LUMO and β-HOMO−3) are significantly lowered due to the nitrogen cation (Figures 6b and S17). Therefore, the energy difference between the α-HOMO and α-LUMO of **2a**$^+$ is reduced to 2.42 eV, while that between β-HOMO and β-LUMO of **2a**$^+$ is increased to 4.35 eV, and its $T_0 \rightarrow T_1$ transition becomes symmetry-allowed. TD-DFT calculations showed that the $T_0 \rightarrow T_1$ transitions of **2a**$^+$ originate from degenerate α-HOMOs → α-LUMO expected at 778 nm with the oscillator strengths of 0.0216, which is longer and stronger than those of **1a** (474 nm, f = 0.0004). $T_1 \rightarrow T_0$ transition of **2a**$^+$ is also allowed (858 nm, f = 0.0115), which is in contrast to the forbidden $T_1 \rightarrow T_0$ transition of **1a** (500 nm, f = 0.0001). These results show that breaking the alternancy symmetry is important to make the $T_0 \rightarrow T_1$ and $T_1 \rightarrow T_o$ transitions allowed and the decrease of the energy level of α-LUMO contributes to the longer-wavelength absorption and fluorescence of **2b**$^+$·TfO$^-$.

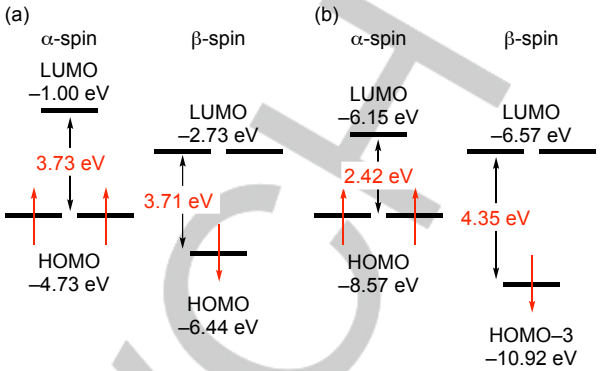

Figure 6. Energies of frontier molecular orbitals of **1a** (a) and **2a**$^+$ (b).

Conclusion

We designed, synthesized, and isolated a kinetically stabilized nitrogen-doped triangulene derivative **2b**$^+$·TfO$^-$ and elucidated its structure and magnetic, electrochemical, and photophysical properties in detail. The replacement of the central carbon atom of the triangulene core with a nitrogen cation does not significantly change the magnetic properties but changes its electrochemical and optical properties. **2b**$^+$·TfO$^-$ is relatively stable under ambient conditions and has a large ΔE_{ST} comparable to a triangulene derivative **1b**. Because the nitrogen cation breaks the alternancy symmetry of **1b** and makes the $T_0 \rightarrow T_1$ transition and $T_1 \rightarrow T_0$ fluorescence allowed and decreases the energy level of α-LUMO, **2b**$^+$·TfO$^-$ exhibited near-infrared absorption and fluorescence. Breaking the alternancy symmetry of alternant hydrocarbon diradicals with a triplet ground state by replacing its appropriate carbon atom with a nitrogen cation would therefore be an effective strategy to create various stable diradicals possessing magnetic properties similar to the parent hydrocarbons but with different electrochemical and photophysical properties.

Acknowledgements

This work was partially supported by JSPS KAKENHI grant number JP20H02723 (A.S.), JP21H01888, JP21H05395, JP23H03956, JP23H04877 (H.S.), JP21H01889, JP21K18934 (H.M.), and JP16K05778 (S.Y.), JST CREST grant number JPMJCR20R3 (A.S.), the AOARD Scientific Project on “Molecular Spins for Quantum Technologies” (FA2386-17-1-4040, 4041), U.S., and the Research Foundation for Opto-Science and Technology (H.S.). We are grateful to Dr. Hiroyasu Sato (Rigaku Corporation) for X-ray crystallographic analysis and Prof. Rainer Herges (Christian-Albrechts-University) for providing the ACID 2.0.1 program. The computations were performed using the Research Center for Computational Science, Okazaki, Japan (Project: 22-IMS-C159).

Conflict of Interest

The authors declare no competing financial interest.

Data Availability Statement

The data that support the findings of this study are available in the Supporting Information of this article.

Keywords: Diradicals, Polycycles, Triangulene, Triplet Ground State, NIR Fluorescence

[1] O. Ostroverkhova, *Chem. Rev.* **2016**, *116*, 13279–13412.
[2] J. Gierschner, J. Shi, B. Milián-Medina, D. Roca-Sanjuán, S. Varghese, S. Y. Park, *Adv. Optical Mater.* **2021**, *9*, 2002251.
[3] R. Matsuoka, A. Mizuno, T. Mibu, T. Kusamoto, *Coord. Chem. Rev.* **2022**, *467*, 214616.
[4] Z. Cui, A. Abdurahman, X. Ai, F. Li, *CCS Chem.* **2020**, *2*, 1129–1145.
[5] L. Ji, J. Shi, J. Wei, T. Yu, W. Huang, *Adv. Mater.* **2020**, *32*, 1908015.
[6] V. Gamero, D. Velasco, S. Latorre, F. López-Calahorra, E. Brillas, L. Juliá, *Tetrahedron Lett.* **2006**, *47*, 2305–2309.
[7] D. Velasco, S. Castellanos, M. López, F. López-Calahorra, E. Brillas, L. Julia, *J. Org. Chem.* **2007**, *72*, 7523–7532.
[8] A. Heckmann, S. Dummler, J. Pauli, M. Margraf, J. Kohler, D. Stich, C. Lambert, I. Fischer, U. Resch-Genger, *J. Phys. Chem. C* **2009**, *113*, 20958–20966.
[9] Q. Jin, S. Chen, Y. Sang, H. Guo, S. Dong, J. Han, W. Chen, X. Yang, F. Li, P. Duan, *Chem. Commun.* **2019**, *55*, 6583–6586.
[10] Y. Hattori, E. Michail, A. Schmiedel, M. Moos, M. Holzapfel, I. Krummenacher, H. Braunschweig, U. Müller, J. Pflaum, C. Lambert, *Chem. Eur. J.* **2019**, *25*, 15463–15471.
[11] E. Cho, V. Coropceanu, J.-L. Brédas, *J. Am. Chem. Soc.* **2020**, *142*, 17782–17786.
[12] Y. Hattori, T. Kusamoto, H. Nishihara, *Angew. Chem. Int. Ed.* **2014**, *53*, 11845–11848; *Angew. Chem.* **2014**, *126*, 12039–12042.
[13] S. Kimura, A. Tanushi, T. Kusamoto, S. Kochi, T. Sato, H. Nishihara, A *Chem. Sci.* **2018**, *9*, 1996–2007.
[14] S. Kimura, M. Uejima, W. Ota, T. Sato, S. Kusaka, R. Matsuda, H. Nishihara, T. Kusamoto, *J. Am. Chem. Soc.* **2021**, *143*, 4329–4338.
[15] S. Kimura, R. Matsuoka, S. Kimura, H. Nishihara, T. Kusamoto, *J. Am. Chem. Soc.* **2021**, *143*, 5610–5615.
[16] T. Kushida, S. Shirai, N. Ando, T. Okamoto, H. Ishii, H. Matsui, M. Yamagishi, T. Uemura, J. Tsurumi, S. Watanabe, J. Takeya, S. Yamaguchi, *J. Am. Chem. Soc.* **2017**, *139*, 14336–14339.
[17] M. Ito, S. Shirai, Y. Xie, T. Kushida, N. Ando, H. Soutome, K. J. Fujimoto, T. Yanai, K. Tabata, Y. Miyata, H. Kita, S. Yamaguchi, *Angew. Chem. Int. Ed.* **2022**, *61*, e202201965; *Angew. Chem.* **2022**, *134*, e202201965.
[18] A. Abdurahman, T. J. H. Hele, Q. Gu, J. Zhang, Q. Peng, M. Zhang, R. H. Friend, F. Li, E. W. Evans, *Nat. Mater.* **2020**, *19*, 1224–1229.
[19] M. Abe, *Chem. Rev.* **2013**, *113*, 7011–7088.
[20] R. Breslow, P. Maslak, J. S. Thomaides, *J. Am. Chem. Soc.* **1984**, *106*, 6453–6454.
[21] T. J. LePage, R. Breslow, *J. Am. Chem. Soc.* **1987**, *109*, 6412–6421.
[22] A. Rajca, K. Shiraishi, S. Rajca, *Chem. Commun.* **2009**, 4372–4374.
[23] P. J. Boratyński, M. Pink, S. Rajca, A. Rajca, *Angew. Chem. Int. Ed.* **2010**, *49*, 5459–5462; *Angew. Chem.* **2010**, *122*, 5591–5594.
[24] K. Kato, K. Furukawa, A. Osuka, *Angew. Chem. Int. Ed.* **2018**, *57*, 9491–9494; *Angew. Chem.* **2018**, *130*, 9635–9638.
[25] C. Shu, H. Zhang, A. Olankitwanit, S. Rajca, A. Rajca, *J. Am. Chem. Soc.* **2019**, *141*, 17287–17294.
[26] S. Tang, L. Zhang, H. Ruan, Y. Zhao, X. Wang, *J. Am. Chem. Soc.* **2020**, *142*, 7340–7344.
[27] H. Namai, H. Ikeda, Y. Hoshi, N. Kato, Y. Morishita, K. Mizuno, *J. Am. Chem. Soc.* **2007**, *129*, 9032–9036.
[28] Z. Feng, Y. Chong, S. Tang, Y. Fang, Y. Zhao, J. Jiang, X. Wang, *Chem. Sci.* **2021**, *12*, 15151–15156.
[29] Its small singlet-triplet energy gap (ΔE_{ST}) of 126.6 K (1.053 kJ mol^{-1}) makes it difficult to elucidate the origin of its fluorescence because the population of thermally-excited singlet state with ΔE_{ST} of 126.6 K is calculated to be 17.9% at 25 °C on the basis of the Boltzmann distribution.
[30] S. Arikawa, A. Shimizu, D. Shiomi, K. Sato, R. Shintani, *J. Am. Chem. Soc.* **2021**, *143*, 19599–19605.
[31] A. Shimizu, T. Morikoshi, K. Sugisaki, D. Shiomi, K. Sato, T. Takui, R. Shintani, *Angew. Chem. Int. Ed.* **2022**, *61*, e202205729; *Angew. Chem.* **2022**, *134*, e202205729.
[32] At the same time of our study on **1b**, Juríček et al. reported the synthesis and characterization of **1c**. L. Valenta, M. Mayländer, P. Kappeler, O. Blacque, T. Šolomek, S. Richert, M. Juríček, *Chem. Commun.* **2022**, *58*, 3019–3022.
[33] G. Trinquier, N. Suaud, J.-P. Malrieu, *Chem. Eur. J.* **2010**, *16*, 8762–8772.
[34] E. Clar, D. G. Stewart, *J. Am. Chem. Soc.* **1953**, *75*, 2667–2673.
[35] E. Clar, D. G. Stewart, *J. Am. Chem. Soc.* **1954**, *76*, 3504–3507.
[36] N. Pavliček, A. Mistry, Z. Majzik, N. Moll, G. Meyer, D. J. Fox, L. Gross, *Nat. Nanotechnol.* **2017**, *12*, 308–312.
[37] J. Inoue, K. Fukui, T. Kubo, S. Nakazawa, K. Sato, D. Shiomi, Y. Morita, K. Yamamoto, T. Takui, K. Nakasuji, *J. Am. Chem. Soc.* **2001**, *123*, 12702–12703.
[38] M. E. Sandoval-Salinas, A. Carreras, D. Casanova, *Phys. Chem. Chem. Phys.* **2019**, *21*, 9069–9076.
[39] T. Wang, A. Berdonces-Layunta, N. Friedrich, M. Vilas-Varela, J. P. Calupitan, J. I. Pascual, D. Peña, D. Casanova, M. Corso, D. G. de Oteyza, *J. Am. Chem. Soc.* **2022**, *144*, 4522–4529.
[40] H. Wei, X. Hou, T. Xu, Y. Zou, G. Li, S. Wu, Y. Geng, J. Wu, *Angew. Chem., Int. Ed.* **2022**, *61*, e202210386; *Angew. Chem.* **2022**, *134*, e202210386.
[41] M. R. Talipov, M. M. Hossain, A. Boddeda, K. Thakur, R. Rathore, *Org. Biomol. Chem.* **2016**, *14*, 2961–2968.
[42] A. N. Sobolev, V. K. Belsky, I. P. Romm, N. Y. Chernikova, E. N. Guryanova, *Acta Crystallogr. Sect. C* **1985**, *C41*, 967–971.
[43] A. Shimizu, Y. Ishizaki, S. Horiuchi, T. Hirose, K. Matsuda, H. Sato, J. Yoshida, *J. Org. Chem.* **2021**, *86*, 770−781.
[44] K. B. Wiberg, *Tetrahedron* **1968**, *24*, 1083–1096.
[45] A. E. Reed, L. A. Curtiss, F. Weinhold, *Chem. Rev.* **1988**, *88*, 899–926.
[46] P. v. R. Schleyer, C. Maerker, A. Dransfeld, H. Jiao, N. J. R. van Eikema Hommes, *J. Am. Chem. Soc.* **1996**, *118*, 6317–6318.
[47] Z. Chen, C. S. Wannere, C. Corminboeuf, R. Puchta, P. v. R. Schleyer, *Chem. Rev.* **2005**, *105*, 3842–3888.
[48] P. v. R. Schleyer, M. Manoharan, Z. Wang, B. Kiran, H. Jiao, R. Puchta, N. J. R. van Eikema Hommes, *Org. Lett.* **2001**, *3*, 2465–2468.
[49] R. Herges, D. Geuenich, *J. Phys. Chem. A* **2001**, *105*, 3214–3220.
[50] D. Geuenich, K. Hess, F. Köhler, R. Herges, *Chem. Rev.* **2005**, *105*, 3758–3772.
[51] H. M. McConnell, *J. Chem. Phys.* **1956**, *24*, 764–766.
[52] N. Hirota, C. A. Hutchison, P. Palmer, *J. Chem. Phys.* **1964**, *40*, 3717–3725.
[53] A. V. Astashkin, A. Schweiger, *Chem. Phys. Lett.* **1990**, *174*, 595–602.
[54] K. Sato, M. Yano, M. Furuichi, D. Shiomi, T. Takui, K. Abe, K. Itoh, A. Higuchi, K. Katsuma, Y. Shirota, *J. Am. Chem. Soc.* **1997**, *119*, 6607–6613.
[55] H. Zhang, M. Pink, Y. Wang, S. Rajca, A. Rajca, *J. Am. Chem. Soc.* **2022**, *144*, 19576–19591.
[56] R. McWeeny, Y. Mizuno, *Proc. R. Soc. London, Ser. A*, **1961**, *259*, 554–577.
[57] The temperature dependence of $\chi_p T$ exhibits hysteretic behavior below 50 K as shown in Figure S11. A significant difference was observed between the $\chi_p T$ values measured after the zero-field-cooled (ZFC) process and those under the field-cooled (FC) condition below 50 K. Some sample dependence has been observed in the magnitude of the deviation and the temperature below which the deviation appears. This indicates that the hysteretic behavior of ZFC and FC susceptibilities results from the absorbed oxygen instead of the bulk ensemble of **2b**$^{+}$·TfO^{-}. Although the origin of the hysteretic anomaly remains unclear

at present, the triplet ground state for **2b**$^{+\cdot}$TfO^{-} giving the $\chi_P T$ value close to 1.00 emu K mol^{-1} is unquestionable.

[58] C. T. Jackson, S. Jeong, G. F. Dorlhiac, M. P. Landry, *iScience* **2021**, *24*, 102156.

[59] M. J. S. Dewar, H. C. Longuet-Higgins, *Proc. Phys. Soc. A.* **1954**, *67*, 795–804.

[60] H. C. Longuet-Higgins, J. A. Pople, *Proc. Phys. Soc. A.* **1955**, *68*, 591–600.

Entry for the Table of Contents

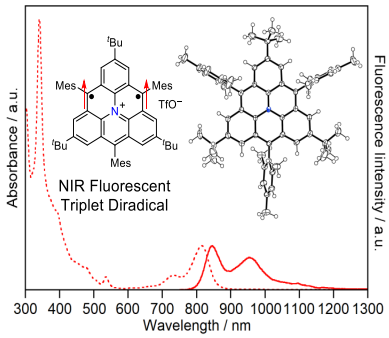

A kinetically-stabilized nitrogen-doped triangulene cation derivative has been synthesized and isolated. It is highly stable even in solution under air and has a triplet ground state with a large singlet-triplet energy gap. In contrast to the triangulene derivative, the nitrogen-doped triangulene cation derivative exhibits near-infrared absorption and emission because the alternancy symmetry of triangulene is broken by the nitrogen cation.